Dynamic equilibrium behaviour observed on two contrasting tidal flats from daily monitoring of bed-level changes

Zhan Hu[a,b,c,*], Daphne van der Wal[d], Huayang Cai[a,b,c], Jim van Belzen[d], Tjeerd J. Bouma[d,e]

[a] Institute of Estuarine and Coastal Research, School of Marine Science, Sun Yat-sen University, Guangzhou 510275, China

[b] State-province Joint Engineering Laboratory of Estuarine Hydraulic Technology, Guangzhou 510275, China

[c] Guangdong Province Engineering Research Center For Coasts, Islands and Reefs, Guangzhou 510275, China

[d] NIOZ Royal Netherlands Institute for Sea Research, department of Estuarine and Delta Systems, and Utrecht University, P.O. Box 140, 4400 AC, Yerseke, The Netherlands

[e] Faculty of Science and Engineering, Groningen University, PO Box 72, 9700 AB Groningen, The Netherlands

* Corresponding author:

Zhan Hu (huzh9@mail.sysu.edu.cn), Tel: +86 (0)20 393 332 62
Address: No. 135, Xingang Xi Road, Guangzhou 510275, China

E-mail addresses of other authors:

Daphne van der Wal (Daphne.van.der.Wal@nioz.nl); Huayang Cai (caihy7@mail.sysu.edu.cn);

Jim van Belzen (Jim.van.Belzen@nioz.nl); Tjeerd J. Bouma (Tjeerd.Bouma@nioz.nl)

Highlights:

- High-resolution field data supports dynamic equilibrium theory for tidal flats
- Empirical Orthogonal Function analysis revealed dynamic equilibrium behaviour
- Tide-induced bottom shear stress shown to regulate morphology of macrotidal systems
- Lower sediment input may have induced the observed pattern of erosion

Abstract

Dynamic Equilibrium Theory (DET) has been applied to tidal flats to systematically explain intertidal morphological responses to various distributions of bed shear stress (BSS). However, it is difficult to verify this theory with field observations because of the discrepancy between the idealized conceptions of theory and the complex reality of intertidal dynamics. The core relation between intertidal morphodynamics and BSS distribution can be easily masked by noise in complex datasets, leading to conclusions of insufficient field evidence to support DET. In the current study, hydrodynamic and morphodynamic data were monitored daily for one year on two tidal flats with contrasting wave exposures. BSS distribution was obtained by validated numerical models. Tidal flat dynamic equilibrium behaviour and BSS were linked via Empirical Orthogonal Function (EOF) analysis. We show that the principal morphodynamic modes corresponded well with the respective modes of BSS found at both sites. Tide-induced BSS was the dominant force at both sites, regardless of the level of wave exposure. The overall erosional and steepening trend found at the two flats can be attributed to the prevailing action of tidal forcing and reduced sediment supply. Hence, EOF analysis confirmed that tidal flat morphodynamics are consistent with DET, providing both field and model evidence to support this theory.

Keywords

Dynamic equilibrium theory; Tidal flats; Bed shear stress; EOF analysis

Introduction

Tidal flat morphology is continuously shaped by diverse physical and biological processes, e.g. tidal currents, wind waves, variability in sediment supply and bioturbation/bioaggregation (Le Hir et al., 2000, 2007; Friedrichs, 2011; Green and Coco, 2007; Talke and Stacey, 2008; Stanev et al., 2009; Green and Coco, 2014; Hunt et al., 2016; Duran-Matute et al., 2016). The long-term dynamics of bare tidal flats is widely recognized as being important in the overall sustainability of coastal ecosystems, such as saltmarshes and mangroves (Fagherazzi et al., 2006; van der Wal et al., 2008; Mariotti and Fagherazzi, 2010, 2013). Recent studies have also identified the short-term dynamics of bed level as a major physical disturbance constraining the establishment of intertidal biotas (Bouma et al., 2001, 2016; Nambu et al., 2012; Balke et al., 2013, 2014, 2015). Thus, understanding intertidal morphodynamics is key to preserving ecosystems and their various services (Barbier et al., 2008; Arkema et al., 2015).

Dynamic equilibrium theory (DET) has been proposed to systematically explain the morphological responses of intertidal systems to tidal and wave-induced forcing over various timescales (Friedrichs and Aubrey, 1996; Friedrichs, 2011) (Fig. 1). DET assumes that tidal flat morphological equilibrium is achieved when the maximum bed shear stress (BSS) is uniform over space, ensuring zero net sediment transport (Friedrichs and Aubrey, 1996; Friedrichs, 2011). Based on this assumption, tidal-dominated (convex) or wave-dominated (concave) profiles of tidal flat equilibrium can be predicted from corresponding BSS distributions. DET further illustrates that under varying BSS, the actual tidal flat profile approximates a dynamic equilibrium over long timescales, situated somewhere between the purely tide-dominated and wave-dominated extremes. Over shorter timescales, tidal-flat morphology may be attracted to one or the other extreme depending on BSS variability (Fig. 1). DET can potentially function as a unifying concept in that it systematically illustrates the relation between prevailing mode of hydrodynamic forcing (in the form of BSS) and intertidal morphodynamics. Other drivers are also

included in the DET framework, such as external sediment supply, bioturbation/ bioaggregation, and human interference (Friedrichs, 2011).

As such, DET is an important theory in understanding and predicting intertidal morphodynamics. However, it is usually difficult to link or test DET with field observations because of the clear discrepancies between theoretical schematization and the complex reality of intertidal morphodynamics. As a result, most of the evidence used to support DET are based on numerical modelling, which involves intrinsic abstraction of intertidal sediment dynamics (Liu et al., 2011; Pritchard et al., 2002; van der Wegen and Jaffe, 2014; Hu et al., 2015a; Maan et al., 2015), while there is much less direct field evidence supporting DET (Wang et al., 1999; Yang et al., 2003; Bearman et al., 2010; Ni et al., 2014) . The reason that fewer field studies have addressed this topic may be attributed to the difficulties in obtaining data sets taken over a sufficient length of time and with adequate spatiotemporal resolution, as well as the difficulty in analysing these complex data sets. In the few field studies supporting DET, intertidal profile shape and morphodynamic behaviours were examined in detail with extensive observations (Yang et al., 2003; Bearman et al., 2010). However, the driving force, i.e. BSS, was not quantified in concert with intertidal morphological evolution in these studies; thus, the correlation between BSS distribution and intertidal bed-level evolution, which sits at the core of DET, remains unverified.

In this study, we aim to provide combined field and modelling evidence for DET by quantitatively linking tidal flat dynamic equilibrium behaviour to BSS distribution. Hydrodynamic and bed-level monitoring was conducted daily for a year (20-Nov-2013 to 20-Nov-2014) on two tidal flats with contrasting wave exposure in the Westerschelde Estuary, the Netherlands (Fig. 2). Newly-developed SED-sensors (Surface Elevation Dynamic sensors) were installed at 12 stations to obtain high-frequency data on bed-level dynamics (Hu et al., 2015b). Wave and tidal current data were measured simultaneously and used to quantify BSS. The main components of BSS were

identified, as well as the relative importance of tidal and wave forcing at these two sites, using Empirical orthogonal function (EOF) analysis. In order to demonstrate the underlying dynamic equilibrium behaviour, the main components of bed-level dynamics were also identified via EOF and analysed in parallel with BSS. Finally, the effect of lower sediment supply on the overall morphological trend at these two tidal flats is discussed.

2. Materials and methods

2.1 Field measurements

The two studied tidal flats in the Westerschelde Estuary have relatively fine sediment, with a median sediment grain size (D50) of 72.1 μm at Zuidgors and 26.8 μm at Baarland. The instrument set-up to measure bed level is shown in Fig. 2. This year-long daily bed-level monitoring was realized by SED-sensors (Surface Elevation Dynamics sensor), recently developed by the Royal Netherlands Institute for Sea Research (NIOZ) (Hu et al., 2015b). The precision of the SED-sensor is ±2 mm and was compared with a precise manual measurement method (sedimentation erosion bars) in an earlier study, with excellent agreement between these two measurements (Hu et al., 2015b). SED-sensors rely on daylight and do not work when submerged by turbid water. The measuring windows of SED-sensors thus occur during "dry" periods under daylight conditions. In the current study, these sensors generally had 1-2 measuring windows per day, depending on the tide level. In each window, one valid data point was recorded to track the bed-level. When there were no bed-level data due to sensor failure, we substituted Differential GPS data obtained at monthly intervals. The DGPS measurement were surveyed manually on these two studied tidal flats. Even though the precision of the DGPS data is lower than for SED-sensors, typically in the range of 5-10 mm (Nolte et al., 2013), we used them as the

only other option during SED-sensor failure.

Besides bed-level measurements, pressure sensors (OSSI-010-003C; Ocean Sensor Systems, Inc.) were used to simultaneously obtain tidal level and wave height data at the measuring frequency of 5 Hz. The measuring interval and the measuring period for each interval were 15 minutes and 7 minutes, respectively. In a measurement interval, time-averaged water depth and bulk wave parameters (peak wave period and significant wave height) were derived by a MATLAB routine based on the standard calculation methods of Tucker and Pitt (2001). This MATLAB routine is available online along with detailed descriptions of the method (at http://neumeier.perso.ch/matlab/waves.html). The depth-averaged velocity data were obtained using ADCPs (Acoustic Doppler Current Profiler) manufactured by Nortek with 2MHz heads (Aquadopp Profilers, http://www.nortek-as.com/lib/brochures/aquadopp-profiler/view). The Aquadopp Profilers were deployed in the seabed with their heads near the bed surface to ensure upward-facing measurements. The blanking distance was 0.1 m. The measuring cells were located 0.1 m apart from each other in the water column, and the total number of cells depends on the actual water depth. The measuring frequency and interval were 0.2 Hz and 10 mins, respectively. The velocity was measured for two complete spring-neap cycles (19-Dec-2013 to 16-Jan-2014).

2.2 Hydrodynamic modelling and BSS quantification

Hydrodynamic parameters, including cross-shore and long-shore current as well as wave height, were quantified by numerical models. The modelling results were subsequently used to quantify BSS. The modelling of cross-shore and long-shore current was conducted following the method described in Le Hir et al. (2000). We calculated the long-shore tidal current at the seaward boundary using a package of MATLAB routines called T_TIDE (Pawlowicz et al., 2002), which detects the main tidal constituents in the ADCP velocity data via harmonic analysis and

subsequently generates time series of velocity data for given periods. Wave modelling was conducted using the 1D SWAN (Simulating WAves Nearshore) model (Booij et al., 1999) at each site. The applied tidal current and wave models have been successfully applied to the same study area in previous studies (Hu et al., 2015a; 2015c) and were validated again using on-site hydrodynamic measurements in the current study. Details of the hydrodynamic model setup and their validation are included in Appendix A.

Tidal and wave-induced BSS (τ_c and τ_w) as well as the maximum combined BSS from current and wave ($\tau_{\max}$) were quantified following Soulsby (1995). BSS over each tidal cycle is represented by the 90th percentile value in the corresponding BSS time series, which has been found to be a useful measure for both peak forcing magnitude and its duration (Friedrichs, 2011; Hu et al., 2015a).

2.3 EOF analysis

In order to facilitate EOF analysis, the obtained data on the 90th percentile BSS values over each tide and bed-level dynamics were interpolated to obtain a constant one-day interval (Miller and Dean, 2007). The main advantage of working with interpolated data is that the resulting temporal eigenfunctions have a constant interval, which facilitates subsequent mode reconstruction and spectral analysis. EOF analysis uses a separation of variables approach to isolate the temporal and spatial dependence of the data (Miller and Dean, 2007). The original matrix $y(x,t)$ can be represented by a series of linear combinations of temporal and spatial functions:

$$y(x,t) = \sum_{k=1}^{n} c_k(t) e_k(x) \qquad (1)$$

in which $c_k(t)$ and $e_k(x)$ are the temporal and spatial eigenfunctions, respectively; k=1 to n, where n is the least of the number of temporal (n_t) and spatial (n_x)samples; and $c_k(t)e_k(x)$ is the reconstructed kth mode of the original data set. The importance of modes decreases with

mode order. The temporal eigenfunctions can be further separated as the following:

$$c_k(t) = a_k c'_k(t) \qquad (2)$$

where $c'_k(t)$ is the normalized temporal eigenfunctions; and a_k is a normalizing factor with $a_k = \sqrt{\lambda_k n_x n_t}$, where λ_k is the eigenvalue associated with the *k*th eigenfunction, which represents the contribution of the *k*th mode to the total variance. The relative contribution of the *k*th mode is given by the following:

$$p_k = \left(\lambda_k \Big/ \sum_{k=1}^{n} \lambda_k \right) \times 100 \qquad (3)$$

The obtained p_k of each mode indicates its respective importance. As mentioned above, the first few modes typically contain the most signals with high p_k .

3. Results

3.1 Daily bed-level dynamics and BSS

At both sites, high-frequency bed-level monitoring and BSS modelling showed that there is great spatiotemporal complexity in both intertidal bed-level dynamics and hydrodynamic forcing (Fig. 3). No apparent dynamic equilibrium behaviour was observed. At the upper stations (Z1-Z6 and B1-B2) with low BSS, there was no apparent trend of erosion and some stations showed net deposition. At the lower stations (Z7-Z9 and B3) with high BSS, net erosion was observed over the one-year monitoring period. Furthermore, the BSS at the lower stations (Z8-Z9 and B2-B3) generally showed two peaks in a month, which could correspond to spring-neap circles, whereas the BSS at upper stations of the exposed site (Z1-Z7) seemed to vary more randomly.

3.2 Percentage of the total variability represented by the first three eigenfunctions

Results of the EOF analysis are summarized in Table 1, which shows that the first few eigenfunctions explained the majority of variation in bed dynamics and BSS at each site. The first

two eigenfunctions of bed-level dynamics described more than 90% of the total variance of the respective variables (Table 1). As the remaining eigenfunctions showed no recognizable or coherent patterns, they were excluded from all following analyses in order to retain the most parsimonious representation of the data.

3.3 Tidal vs. wave forcing

The EOF analysis of τ_c, τ_w and $\tau_{\max}$ showed that τ_c is the dominating forcing at both sites, regardless of differences in wave exposure (Fig. 4). As the 1st eigenfunctions of τ_c, τ_w and $\tau_{\max}$ explained more than 88% of their respective total variances (Table 1), only the 1st eigenfunctions were analysed and compared. At both sites, the spatial and temporal eigenfunctions of τ_c were very similar to those of $\tau_{\max}$, whereas the eigenfunctions of τ_w were not similar to those of $\tau_{\max}$ (Fig. 4). This indicates that τ_c composed the bulk of $\tau_{\max}$ and that the influence of τ_w on $\tau_{\max}$ was minor at both sites, regardless of wave-exposure condition.

The different wave exposure at the two study sites was however reflected in the temporal eigenfunctions of τ_w. At the sheltered Baarland site, the temporal eigenfunctions of τ_w were consistently close to zero, implying negligible wave forcing (Fig. 4d). At the exposed Zuidgors site, however, the temporal eigenfunction of τ_w showed relatively strong wave forcing during the first 100 days, corresponding to the winter season with larger incident waves (Fig. 4c). At this site, the spatial eigenfunction of τ_w peaked at Z6, where breaking waves were frequent (Fig. 4a).

3.4 Relation between $\tau_{\max}$ and bed-level dynamics based on EOF analysis

In order to examine the relation between $\tau_{\max}$ distribution and bed-level dynamics, their spatial eigenfunctions were analysed for correlation (Fig. 5). For both sites, the 1st and 2nd spatial eigenfunctions of bed-level dynamics showed strong correlations with the corresponding eigenfunctions of $\tau_{\max}$. This indicates that the main intertidal morphodynamic trend is closely linked to BSS distribution. The correlation coefficients were all negative, supporting the DET

principle that strong forcing leads to erosional trends and weak forcing leads to depositional trends. At the Zuidgors site, the correlations between bed-level dynamics and τ_{max} were significant for both the 1st (r = -0.90, p = 0.04<0.05) and 2nd (r = -0.97, p = 0.01<0.05) spatial eigenfunctions (Fig. 5a, 5c). The original data was subsampled prior to correlation analysis in order to avoid spatial autocorrelation (Appendix B).

At the Baarland site, the correlations between bed-level dynamics and τ_{max} were r=-0.99, p=0.10>0.05 for the 1st eigenfunctions and r=-0.95, p=0.21>0.05 for the 2nd eigenfunctions, respectively (Fig. 5b, 5d). The statistically insignificant correlations (p>0.05) were probably related to lack of power due to small sample sizes (n=3). Nonetheless, the obtained high r-values show considerable correlation between the spatial eigenfunctions of bed-level dynamics and τ_{max}. Furthermore, it is noted that at both sites, the 1st spatial eigenfunctions of τ_{max} and bed-level dynamics are consistent with the tidal-dominated profiles as described in Fig. 1.

The temporal eigenfunctions of bed-level dynamics may seem chaotic (e.g. Fig. 4c, 4d and insets in Fig. 5), but spectral analysis revealed that the main temporal fluctuations ($c_1(t)$ and $c_2(t)$) of τ_{max} and bed-level dynamics coincided with each other (Fig. 6). For both sites, the peaks in the spectrum of the 1st τ_{max} temporal eigenfunctions were at frequencies close to zero, which corresponds to inter-annual variations (Fig. 6a, 6b). Similar peaks in the spectrum close to zero frequency were also observed in the spectrum of the 1st bed-level temporal eigenfunctions (Fig. 6c, 6d). The similarity in τ_{max} and bed-level temporal eigenfunctions indicates that the temporal variation in hydrodynamic forcing exerted a strong impact on intertidal morphodynamics, and the temporal variations of both hydrodynamic forcing and bed-level had time scales longer than one year. Similar correspondence was also found in the spectrum of the 2nd τ_{max} and bed-level temporal eigenfunctions (Fig. 6). For both sites, the peaks in the spectrums of the 2nd eigenfunctions were at the frequency 0.00274 cycles/day, corresponding to annual variations. This

further confirms the regulating role of τ_{max} on bed-level dynamics.

The spectrum of bed-level dynamics did not correspond to the subordinate peaks in the spectrum of τ_{max} temporal eigenfunctions (SP1-SP3 in Fig. 6a, 6b). These subordinate peaks can be recognized as representing lunar-month cycles, spring-neap cycles and 9.6-day cycles in τ_{max}. This indicates that at our study sites, these relatively short-term variations in hydrodynamic forcing have no apparent effect on annual-scale, bed-level dynamics. These subordinate peaks in the τ_{max} spectrum likely stemmed from tidal constituents detected by T_TIDE (Appendix A).

Combined eigenfunctions (reconstructed modes) were quantified to synthesize the spatiotemporal variations of bed-level dynamics and τ_{max} (Fig. 7). These combined eigenfunctions further show that bed-level dynamics at both sites were closely linked to the corresponding modes of BSS. The 1st modes of bed-level dynamics at both sites showed overall erosion and steepening trends (Fig. 7a, 7b). The steepening trend at both sites became more apparent towards the end of the monitoring period. These morphodynamic trends are consistent with the spatial distribution of the reconstructed 1st modes of τ_{max}, which were stronger at the lower stations and weaker at the upper stations (Fig. 7c, 7d). This spatial distribution was maintained over time, despite the temporal variation in peak magnitude. This observed linkage in the 1st combined eigenfunctions supports the case of the tide-dominated profiles as depicted in Fig. 1.

The 2nd combined eigenfunctions of bed-level dynamics also corresponded with the matching modes at both sites (Fig. 7e-h). Spatially, most of these dynamics occurred around the middle of both tidal flats (stations Z5-Z6 and B2). The peaks and troughs of the reconstructed τ_{max} were also located at these stations. Temporally, the reconstructed bed-level dynamics showed an annual cycle, i.e. erosion during ca. the first 200 days and deposition during the rest of the period (Fig. 7e-7f). Correspondingly, reconstructed τ_{max} was generally stronger in the first 200 days and weaker during the rest of the monitoring period (Fig. 7g-7h). Thus, both temporal and spatial

modes of the reconstructed τ_{max} were echoed in the reconstructed bed-level dynamics. The reasons for this seasonality will be addressed in the Discussion section.

4. Discussion

4.1 Direct field evidence supporting DET

No prior physical assumptions are made in EOF analysis. Therefore, the resulting modes (eigenfunctions) do not have any predefined physical significance. Yet, EOF analysis showed that the main temporal and spatial modes of bed-level dynamics correspond well with those of BSS. This demonstrates the regulating role of BSS distribution on intertidal morphodynamics, which is consistent with DET (Friedrichs and Aubrey, 1996; Friedrichs, 2011; Hu et al., 2015a). At both sites, tide-induced BSS was the dominant force, and the resulting bed-level dynamics carried a clear signature of tidal dominance, leading to steeper profiles of the tidal flats. Similar steepening trends have been found at many offshore tidal flats (i.e. tidal flats surrounded by water) in the Westerschelde Estuary (de Vet et al., 2017).

Importantly, we have expanded upon previous field studies (Yang et al., 2003; Bearman et al., 2010), and verified that tidal flat dynamic equilibrium behaviour is closely linked to BSS distribution, which is the core principle of DET. Primarily explored by numerical modelling (Pritchard et al., 2002; Liu et al., 2011; van der Wegen and Jaffe, 2014; Hu et al., 2015a; Maan et al., 2015), this correlation has rarely been addressed by field measurements. Thus, the obtained data on daily bed-level dynamics and their strong correlation with simulated hydrodynamic forcing provide combined field and modelling evidence in support of DET.

It is often difficult and costly to obtain high-resolution morphodynamic and BSS data. Additionally, the obtained raw data are generally complex (e.g. see Fig. 3), which may mask the underlying dynamic equilibrium mechanism. In the current study, BSS was calculated using validated hydrodynamic models, and the daily bed-level monitoring was achieved through using

novel SED-sensors (Hu et al., 2015b). These automatic sensors are relatively low-cost and easy to install in field, which makes them suitable for large-scale monitoring programs requiring high spatiotemporal resolution. EOF analysis was successfully employed in the current study to filter noisy data. It was able to identify the main components in hydrodynamic forcing and intertidal morphodynamics, which facilitated subsequent interpretations of the tidal flat dynamic equilibrium behaviours.

The main limitation of the SED-sensors is that they take point measurements. Future studies could combine marine radar technology with SED-sensors to explore tidal flat dynamic equilibrium behaviours over larger scales while maintaining high monitoring resolution (Bell et al., 2016; Bird et al., 2017), and thus lead to improvements in current understanding of DET and morphological modelling.

4.2 Hydrodynamic forcing at two contrasting sites

The respective roles of tidal and wave forcing on intertidal sediment transport and morphodynamics have been frequently discussed in the literature (Allen and Duffy, 1998; Friedrichs, 2011; Green and Coco, 2014; Hu et al., 2015a; Maan et al., 2015; Hunt et al., 2016). Two tidal flats were monitored in the current study to test if different levels of wave exposure can lead to contrasting dynamic equilibrium behaviours. However, despite the dissimilarity in wave exposure, tidal current was identified as the driving force in the two investigated macrotidal sites (mean tidal range>4 m). The dominance of tidal forcing has been identified by previous studies in other macrotidal systems (Allen and Duffy, 1998; Pritchard et al., 2002; Friedrichs, 2011). Wave-induced erosion was apparent during storms at the exposed site (Hu et al., 2015b), which can influence some of the critical ecological processes in the intertidal environments, such as marsh seedling establishment (Balke et al., 2014; Bouma et al., 2016). However, the occurrence of storms at this site was too low to have a strong impact on the overall morphological equilibrium.

This limited influence of storms on long-term morphology was also found in a recent modelling study conducted in the same study area (Dam et al., 2016). The 2nd modes of τ_{max} at both sites showed apparent seasonality. For the exposed Zuidgors site, the seasonality may be partly attributed to seasonal wave forcing (Callaghan et al., 2010). For both sites, this seasonality may be also related to variations in seasonal tidal forcing (lower two panels of Fig. 4). Similar seasonal variations in tidal forcing have been identified in previous studies (Allen and Duffy, 1998; Harrison et al., 2017).

4.3 Sediment supply and management implications

Besides hydrodynamic forcing, tidal flat dynamic equilibrium is also closely related to external sediment supply (Friedrichs, 2011). A recent study has illustrated that mean sediment concentration level determines the uniform BSS of the dynamic equilibrium system (i.e. τ_E in Fig. 1) (Hu et al., 2015a). Conceptually, τ_E defines the exact amount of sediment in the water column needed to maintain a constant sediment concentration in the system, i.e. without losing sediment to the seabed or gaining sediment from the seabed and thus resulting in a morphological equilibrium state. Therefore, the mean sediment concentration and the corresponding τ_E essentially determine the dynamic equilibrium of a tidal flat over the considered timescale. This is logical as the mean sediment concentration level in a study area generally accounts for various effects, including local hydrodynamic forcing, sediment supply as well as bioturbation/bioaggregation, which can be regarded as a synthetic indicator for intertidal equilibrium. When the external sediment supply increases or decreases, τ_E varies accordingly. As shown in Fig. 1, when τ_E increases or decreases, the trend of deposition or erosion changes even though τ_c or τ_w is kept constant. Thus, external sediment supply can effectively influence tidal flat dynamic equilibrium behaviour (Friedrichs, 2011). It should be noted that idealization of τ_E to reach morphological equilibrium ignores Eulerian (i.e., local, time-dependent) asymmetries, e.g. asymmetrical flood/ebb peak velocities. This stems from the compact concept

of DET, which neglects Eulerian asymmetries and focuses only on Lagrangian (spatial) asymmetries (Friedrichs, 2011). As the aim of our study is to find evidence of DET, we adopted the same assumptions as DET.

At our study sites, sediment supply was probably high in the period 1997-2005, due to transport of dredged sediment disposed just west of the Zuidgors site, and this supply is now likely in decline. Therefore, even when encountering the same level of forcing, these tidal flats are more prone to erosion, which may explain the observed general trend in bed-level dynamics at both sites. Bed erosion undermines coastal defence and the ecological values of tidal flats (Callaghan et al., 2010; Temmerman et al., 2013; Bouma et al., 2016). Therefore, it is important to maintain a sufficient level of sediment supply to prevent long-term erosion. Sediment supply is generally determined by larger-scale processes, in which numerous natural and anthropogenic factors play roles. For example, sediment supply in the Yangtze River Estuary has decreased dramatically due to upstream damming, which poses a great challenge to coastal management (Yang et al., 2006; Dai and Liu, 2013; Dai et al., 2014, 2016). As a countermeasure, it may be beneficial to use dredged sediment to nourish tidal flats. A pilot project in the Netherlands has shown that tidal flat nourishment is effective in mitigating erosion (van der Werf et al., 2015), and this result is worthy of further experimentation.

5. Conclusions

The current study has expanded upon previous field work and indicates that the observed dynamic equilibrium behaviour in these tidal flats is closely linked to modelled BSS distributions. Under the prevailing action of tidal forcing, the intertidal morphodynamic trends supported predictions by DET on both the monitored tidal flats, thus providing combined field and modelling results as evidence. The contrasting wave exposure on the two tidal flats did not result in any apparent differences in the overall BSS distribution pattern and bed-level dynamics. This

implies that tide current plays a larger role than waves in the studied macrotidal system. The overall erosion and steepening trends at both sites was attributed to the combined effect of hydrodynamic forcing and reduced sediment supply. In line with DET, the decline in sediment supply leads to lower levels of the conceptual parameter uniform BSS (τ_E). Consequently, both tidal flats are prone to erosion even if the encountered hydrodynamic forcing is constant. Tidal flat nourishment may be an effective measure to prevent erosion and protect these valuable intertidal ecosystems.

Acknowledgments

This work was financially supported by the National Key R&D Program of China (No. 2016YFC0402601), Joint Research Projects NSFC (No. 51761135022) – NWO (No. ALWSD.2016.026) – EPSRC (No. EP/R024537/1): Sustainable Deltas, the 2017 Guangdong Oceanic and Fishery Department scientific research and technological development program, the STW-NWO (No. 07324), the NWO funded BE-SAFE project (No. 850.13.011), the EU FP7 FAST project (No. 607131) and the Galgeschoor project (No. OC2728). We thank Prof. Y. Pan at Hohai University, Dr. S.Y. Ou and H. Chen at SYSU for the technical support of data analysis.

References

Allen, J.R.L., Duffy, M.J., 1998. Medium-term sedimentation on high intertidal mudflats and salt marshes in the Severn Estuary, SW Britain: The role of wind and tide. Mar. Geol. 150, 1–27. doi:10.1016/S0025-3227(98)00051-6

Arkema, K.K., Verutes, G.M., Wood, S.A., Clarke-Samuels, C., Rosado, S., Canto, M., Rosenthal, A., Ruckelshaus, M., Guannel, G., Toft, J., Faries, J., Silver, J.M., Griffin, R., Guerry, A.D., 2015. Embedding ecosystem services in coastal planning leads to better outcomes for people and nature. Proc. Natl. Acad. Sci. U. S. A. 112, 7390–7395. doi:10.1073/pnas.1406483112

Balke, T., Herman, P.M.J., Bouma, T.J., 2014. Critical transitions in disturbance-driven ecosystems: Identifying windows of opportunity for recovery. J. Ecol. 102, 700–708. doi:10.1111/1365-2745.12241

Balke, T., Swales, A., Lovelock, C.E., Herman, P.M.J., Bouma, T.J., 2015. Limits to seaward expansion of mangroves: Translating physical disturbance mechanisms

into seedling survival gradients. J. Exp. Mar. Biol. Ecol. 467, 16–25. doi:10.1016/j.jembe.2015.02.015

Balke, T., Webb, E.L., van den Elzen, E., Galli, D., Herman, P.M.J., Bouma, T.J., 2013. Seedling establishment in a dynamic sedimentary environment: A conceptual framework using mangroves. J. Appl. Ecol. 50, 740–747. doi:10.1111/1365-2664.12067

Barbier, E.B., Koch, E.W., Silliman, B.R., Hacker, S.D., Wolanski, E., Primavera, J., Granek, E.F., Polasky, S., Aswani, S., Cramer, L.A., Stoms, D.M., Kennedy, C.J., Bael, D., Kappel, C.V., Perillo, G.M.E., Reed, D.J., 2008. Coastal ecosystem-based management with nonlinear ecological functions and values. Science 319, 321–323. doi:10.1126/science.1150349

Bearman, J.A., Friedrichs, C.T., Jaffe, B.E., Foxgrover, A.C., 2010. Spatial trends in tidal flat shape and associated environmental parameters in South San Francisco Bay. J. Coast. Res. 26, 342–349.

Bell, P.S., Bird, C.O., Plater, A.J., 2016. A temporal waterline approach to mapping intertidal areas using X-band marine radar. Coast. Eng. 107, 84–101. doi:10.1016/j.coastaleng.2015.09.009

Bird, C.O., Bell, P.S., Plater, A.J., 2017. Application of marine radar to monitoring seasonal and event-based changes in intertidal morphology. Geomorphology 285, 1–15. doi:10.1016/j.geomorph.2017.02.002

Booij, N., Ris, R.C., Holthuijsen, L.H., 1999. A third-generation wave model for coastal regions 1. Model description and validation. J. Geophys. Res. C Oceans 104, 7649–7666.

Bouma, H., Duiker, J.M.C., De Vries, P.P., Herman, P.M.J., Wolff, W.J., 2001. Spatial pattern of early recruitment of Macoma balthica (L.) and Cerastoderma edule (L.) in relation to sediment dynamics on a highly dynamic intertidal sandflat. J. Sea Res. 45, 79–93. doi:10.1016/S1385-1101(01)00054-5

Bouma, T.J., van Belzen, J., Balke, T., van Dalen, J., Klaassen, P., Hartog, A.M., Callaghan, D.P., Hu, Z., Stive, M.J.F., Temmerman, S., Herman, P.M.J., 2016. Short-term mudflat dynamics drive long-term cyclic salt marsh dynamics. Limnol. Oceanogr. 61, 2261–2275. doi:10.1002/lno.10374

Callaghan, D.P., Bouma, T.J., Klaassen, P., van der Wal, D., Stive, M.J.F., Herman, P.M.J., 2010. Hydrodynamic forcing on salt-marsh development: Distinguishing the relative importance of waves and tidal flows. Estuar. Coast. Shelf Sci. 89, 73–88.

Dai, Z., Fagherazzi, S., Mei, X., Gao, J., 2016. Decline in suspended sediment concentration delivered by the Changjiang (Yangtze) River into the East China Sea between 1956 and 2013. Geomorphology 268, 123–132. doi:10.1016/j.geomorph.2016.06.009

Dai, Z., Liu, J.T., 2013. Impacts of large dams on downstream fluvial sedimentation: An example of the Three Gorges Dam (TGD) on the Changjiang (Yangtze River). J. Hydrol. 480, 10–18. doi:10.1016/j.jhydrol.2012.12.003

Dai, Z., Liu, J.T., Wei, W., Chen, J., 2014. Detection of the Three Gorges Dam influence on the Changjiang (Yangtze River) submerged delta. Sci. Rep. 4, 6600. doi:10.1038/srep06600

Dam, G., van der Wegen, M., Labeur, R.J., Roelvink, D., 2016. Modeling centuries of

estuarine morphodynamics in the Western Scheldt estuary. Geophys. Res. Lett. 43, 3839–3847. doi:10.1002/2015GL066725

de Vet, P.L.M., van Prooijen, B.C., Wang, Z.B., 2017. The differences in morphological development between the intertidal flats of the Eastern and Western Scheldt. Geomorphology 281, 31–42. doi:10.1016/j.geomorph.2016.12.031

Duran-Matute, M., Gerkema, T., Sassi, M.G., 2016. Quantifying the residual volume transport through a multiple-inlet system in response to wind forcing: The case of the western Dutch Wadden Sea. J. Geophys. Res.-Oceans 121, 8888–8903. doi:10.1002/2016JC011807

Fagherazzi, S., Carniello, L., D'Alpaos, L., Defina, A., 2006. Critical bifurcation of shallow microtidal landforms in tidal flats and salt marshes. Proc. Natl. Acad. Sci. U. S. A. 103, 8337–8341.

Fortin, M.-J., Dale, M.R.T., 2005. Spatial Analysis: A Guide for Ecologists. Cambridge University Press.

Friedrichs, C.T., 2011. Tidal Flat Morphodynamics: A Synthesis, in: Wolanski, E., McLusky, D. (Eds.), Treatise on Estuarine and Coastal Science. Academic Press, Waltham, pp. 137–170.

Friedrichs, C.T., Aubrey, D.G., 1996. Uniform bottom shear stress and equilibrium hyposometry of intertidal flats, in: Pattiaratchi, C. (Ed.), Coastal and Estuarine Studies. American Geophysical Union, Washington, D. C., pp. 405–429.

Green, M.O., Coco, G., 2014. Review of wave-driven sediment resuspension and transport in estuaries. Rev. Geophys. 52, 77–117. doi:10.1002/2013RG000437

Green, M.O., Coco, G., 2007. Sediment transport on an estuarine intertidal flat: Measurements and conceptual model of waves, rainfall and exchanges with a tidal creek. Estuar. Coast. Shelf Sci. 72, 553–569.

Harrison, S.R., Bryan, K.R., Mullarney, J.C., 2017. Observations of morphological change at an ebb-tidal delta. Mar. Geol. 385, 131–145. doi:10.1016/j.margeo.2016.12.010

Hu, Z., Wang, Z.B., Zitman, T.J., Stive, M.J.F., Bouma, T.J., 2015a. Predicting long-term and short-term tidal flat morphodynamics using a dynamic equilibrium theory. J. Geophys. Res.-Earth Surf. 120, 1803–1823. doi:10.1002/2015JF003486

Hu, Z., Lenting, W., van der Wal, D., Bouma, T.J., 2015b. Continuous monitoring bed-level dynamics on an intertidal flat: Introducing novel, stand-alone high-resolution SED-sensors. Geomorphology 245, 223–230. doi:10.1016/j.geomorph.2015.05.027

Hu, Z., Van Belzen, J., Van Der Wal, D., Balke, T., Wang, Z.B., Stive, M., Bouma, T.J., 2015c. Windows of opportunity for salt marsh vegetation establishment on bare tidal flats: The importance of temporal and spatial variability in hydrodynamic forcing. J. Geophys. Res. G Biogeosciences 120, 1450–1469. doi:10.1002/2014JG002870

Hunt, S., Bryan, K.R., Mullarney, J.C., Pritchard, M., 2016. Observations of asymmetry in contrasting wave- and tidally-dominated environments within a mesotidal basin: implications for estuarine morphological evolution. Earth Surf. Process. Landf. 41, 2207–2222. doi:10.1002/esp.3985

Le Hir, P., Monbet, Y., Orvain, F., 2007. Sediment erodability in sediment transport modelling: Can we account for biota effects? Cont. Shelf Res. 27, 1116–1142.

Le Hir, P., Roberts, W., Cazaillet, O., Christie, M., Bassoullet, P., Bacher, C., 2000. Characterization of intertidal flat hydrodynamics. Cont. Shelf Res. 20, 1433–1459.

Liu, X.J., Gao, S., Wang, Y.P., 2011. Modeling profile shape evolution for accreting tidal flats composed of mud and sand: A case study of the central Jiangsu coast, China. Cont. Shelf Res. 31, 1750–1760. doi:10.1016/j.csr.2011.08.002

Maan, D.C., Van, P., Wang, Z.B., De, V., 2015. Do intertidal flats ever reach equilibrium? J. Geophys. Res. F Earth Surf. 120, 2406–2436. doi:10.1002/2014JF003311

Mariotti, G., Fagherazzi, S., 2013. A two-point dynamic model for the coupled evolution of channels and tidal flats. J. Geophys. Res. Earth Surf. 118, 1387–1399. doi:10.1002/jgrf.20070

Mariotti, G., Fagherazzi, S., 2010. A numerical model for the coupled long-term evolution of salt marshes and tidal flats. J. Geophys. Res. F Earth Surf. 115.

Miller, J.K., Dean, R.G., 2007. Shoreline variability via empirical orthogonal function analysis: Part I temporal and spatial characteristics. Coast. Eng. 54, 111–131. doi:10.1016/j.coastaleng.2006.08.013

Nambu, R., Saito, H., Tanaka, Y., Higano, J., Kuwahara, H., 2012. Wave actions and topography determine the small-scale spatial distribution of newly settled Asari clams Ruditapes philippinarum on a tidal flat. Estuar. Coast. Shelf Sci. 99, 1–9.

Ni, W., Wang, Y.P., Symonds, A.M., Collins, M.B., 2014. Intertidal flat development in response to controlled embankment retreat: Freiston Shore, The Wash, UK. Mar. Geol. 355, 260–273. doi:10.1016/j.margeo.2014.06.001

Pawlowicz, R., Beardsley, B., Lentz, S., 2002. Classical tidal harmonic analysis including error estimates in MATLAB using T_TIDE. Comput. Geosci. 28, 929–937. doi:10.1016/S0098-3004(02)00013-4

Pritchard, D., Hogg, A.J., Roberts, W., 2002. Morphological modelling of intertidal mudflats: The role of cross-shore tidal currents. Cont. Shelf Res. 22, 1887–1895.

Roberts, W., Le Hir, P., Whitehouse, R.J.S., 2000. Investigation using simple mathematical models of the effect of tidal currents and waves on the profile shape of intertidal mudflats. Cont. Shelf Res. 20, 1079–1097.

Soulsby, R.L., 1995. Bed shear stress due to combined waves and currents, in: Advances in Coastal Morphodynamics. edited by M. J. F. Stive et al., Delft Hydraulics, Delft, The Netherlands, p. 4:20–4:23.

Stanev, E.V., Grayek, S., Staneva, J., 2009. Temporal and spatial circulation patterns in the East Frisian Wadden Sea. Ocean Dyn. 59, 167–181. doi:10.1007/s10236-008-0159-0

Talke, S.A., Stacey, M.T., 2008. Suspended sediment fluxes at an intertidal flat: The shifting influence of wave, wind, tidal, and freshwater forcing @. Cont. Shelf Res. 28, 710–725.

Temmerman, S., Meire, P., Bouma, T.J., Herman, P.M.J., Ysebaert, T., De Vriend, H.J., 2013. Ecosystem-based coastal defence in the face of global change. Nature 504, 79–83. doi:10.1038/nature12859

Tucker, M.J., Pitt, E.G., 2001. Waves in Ocean Engineering, 1 edition. ed. Elsevier Science, Amsterdam ; New York.

van der Wal, D., Wielemaker-Van den Dool, A., Herman, P.M.J., 2008. Spatial patterns, rates and mechanisms of saltmarsh cycles (Westerschelde, The Netherlands). Estuar. Coast. Shelf Sci. 76, 357–368.

van der Wegen, M., Jaffe, B.E., 2014. Processes governing decadal-scale depositional narrowing of the major tidal channel in San Pablo Bay, California, USA. J. Geophys. Res. Earth Surf. 119, 1136–1154. doi:10.1002/2013JF002824

van der Werf, J., Reinders, J., van Rooijen, A., Holzhauer, H., Ysebaert, T., 2015. Evaluation of a tidal flat sediment nourishment as estuarine management measure. Ocean Coast. Manag. 114, 77–87. doi:10.1016/j.ocecoaman.2015.06.006

Wang, Y., Zhang, R., Gao, S., 1999. Geomorphic and hydrodynamic responses in salt marsh-tidal creek systems, Jiangsu, China. Chin. Sci. Bull. 44, 544–549.

Yang, S.L., Friedrichs, C.T., Shi, Z., Ding, P.-X., Zhu, J., Zhao, Q.-Y., 2003. Morphological Response of Tidal Marshes, Flats and Channels of the Outer Yangtze River Mouth to a Major Storm. Estuaries 26, 1416–1425.

Yang, S.L., Li, M., Dai, S.B., Liu, Z., Zhang, J., Ding, P.X., 2006. Drastic decrease in sediment supply from the Yangtze River and its challenge to coastal wetland management. Geophys. Res. Lett. 33.

Appendix A. Validation of hydrodynamic models and BSS quantification

Hydrodynamic models were built to provide complete data sets of tidal currents and waves when there were no measurements available. Wind-wave propagation was simulated using a spectral model, i.e. SWAN (Simulating Waves Nearshore) (Booij et al., 1999). Wave shoaling, breaking, and bottom friction processes on tidal flats were explicitly accounted for in this model. At each site, a 1-D modelling domain was built along the measuring transect (Fig. 2). The spatial resolution of a computation domain is 1 m. Each model domain was forced by incident waves with a Joint North Sea Wave Project spectrum at the seaward boundary (default setting in SWAN), while the wind-induced wave growth was excluded (Hu et al., 2015a). The bulk parameters of the incident waves, i.e. significant wave height and peak wave period, were provided by the most seaward station at each site. In the current study, the default model parameter setting was applied. For more details, please see http://swanmodel.sourceforge.net.

In order to evaluate the performance of the wave model, the modelling results were compared to the measurements obtained from the 9 wave stations during both stormy (20-Nov-2013 to 14-Jan-2014) and calm (13-Jun-2014 to 16-Jul-2014) seasons (Fig. A.1). The measuring interval was 15 minutes. At both sites, the wave modelling results were in good agreement with the obtained measurements. The R^2 value and sampling size (n) at the Zuidgors and Baarland sites were 0.94 (n=19410) and 0.66 (n=8983), respectively.

Cross-shore and long-shore tidal currents were also modelled in the current study. Tidal current modelling shared the same computation domains of those used in wave modelling. Cross-shore current was modelled following water volume conservation, which has been widely used in previous studies (Friedrichs and Aubrey, 1996; Le Hir et al., 2000). As the tide rises, the water line moves landward, resulting in onshore flows. The volume of water that must pass through the vertical long-shore plane at location x must equal the increase of water volume in the landward

direction of the long-shore plane (ΔV). The water volume changes can be readily determined by tracking the tidal level fluctuation, if we assume tidal levels are always horizontal. Subsequently, the cross-shore current (u_c(x)) that causes this ΔV in a time interval of Δt can be determined as the following:

$$u_c(x) = \frac{\Delta V(x)}{\Delta t h(x)} \qquad \text{(A.1)}$$

where $h(x)$ is the local water depth. Bed friction is not included in the quantification of u_c.

The long-shore tidal current velocity is derived following the classic method described in Le Hir et al., (2000). This approach is commonly applied as a simple method to derive long-shore current velocity distribution when long-shore tidal velocity at one particular water depth is known. In our case, this one particular location was at the tidal flat seaward boundary. Long-shore tidal velocity at the seaward boundary (u_{l_sea}) was predicted by a MATLAB package called T_TIDE (Pawlowicz et al., 2002). We firstly used T_TIDE to perform harmonic analysis of the long-shore component of the measured current velocity data at the most seaward station. The harmonic analysis derives local constituents of tidal current velocity. This is similar to the common derivation of tidal constituents using water level data. Then, based on the obtained tidal current constituents, T_TIDE can be applied to generate u_{l_sea} time series at any given time. Finally, the long-shore tidal current at each location (u_l(x)) was quantified by balancing the bed friction distributed over the water column and the long-shore water surface slope in depth-averaged momentum equation following Le Hir et al., (2000). The bed friction was assumed to be proportional to the square of the depth-averaged velocity:

$$(\mathrm{g}\frac{\partial \eta}{\partial y} = -\frac{f_c u_l(x)^2}{h(x)}) \qquad \text{(A.2)}$$

where f_c is a constant friction factor. We further assumed that the water level gradient is uniform on a tidal flat transect, since the tide propagation often has a much larger spatial scale than a

typical transect. Then u_l(x) can be determined as the following:

$$u_l(x) = u_{l\_sea}\sqrt{\frac{h(\mathrm{x})}{h_{sea}}} \qquad \text{(A.3)}$$

where h_{sea} is the water depth at the seaward boundary. The long-shore water levels are assumed to be uniform in space, and they are set as the water levels of the most seaward pressure sensor stations. The total velocity can be determined as the following:

$$u = \sqrt{u_c^2 + u_l^2} \qquad \text{(A.4)}$$

The angle between cross-shore and long-shore current is described by the following equation:

$$\theta = \tan^{-1}(\frac{u_l}{u_c}) \qquad \text{(A.5)}$$

The cross-shore velocity at our study sites is in the order of 0.1 m/s, and the long-shore velocity is in the order of 1 m/s. The cross-shore velocity is much smaller comparing to the long-shore velocity, which is probably due to the small width of the studied tidal flats (40-400 m). At both sites, the velocity modelling results were generally consistent with the measurements (Fig. A.2). The measurements were conducted from 19-Dec-2013 to 16-Jan-2014 at the stations shown in Fig. 2. The measuring interval was 10 minutes. The R^2 value and sampling size (n) of total velocity at Zuidgors and Baarland sites were 0.86 (n=5721) and 0.76 (n=3111), respectively. A relative bias (Rel.bias) is defined as the following:

$$\mathrm{Re}\,l.bias = \frac{\sum_{i=1}^{n}(\Psi^i_{\mathrm{mod}\,el} - \Psi^i_{obs})}{\sum_{i=1}^{n}\Psi^i_{obs}} \qquad \text{(A.6)}$$

The Rel.bias of the tidal current velocity was -0.147 for the Zuidgors site and -0.187 for the Baarland site. Thus, the tidal current models slightly underestimated the tidal current velocity at both sites. Since the modelled velocity was generally in good agreement with the measurements, neglecting bed friction in u_c may not lead to large modelling errors.

Based on the wave and tidal current modelling results, we derive the combined BSS from wave and current following (Soulsby, 1995). The magnitude of BSS induced by current is defined as the following:

$$\tau_c = \rho f_c u^2 \qquad \text{(A.7)}$$

where ρ is water density, and $f_c = 0.002$ is a constant friction factor for currents (Roberts et al., 2000). It is noted that the applied 1D tidal velocity model equals depth-averaged velocity with the near-bed shear velocity, which may lead to some inaccuracy in BSS estimation. However, we think this model can still provide satisfactory enough estimation of BSS for analyzing the link between hydrodynamic forcing and tidal flat dynamic equilibrium. The same assumption has been applied in a number of previous studies on morphodynamic modelling (e.g. Equation 7. of Robert et al., 2000; Equation 15. of Callaghan et al., 2010; Equation 3. of Maan et al., 2015; Equation 6. of Hu et al., 2015b). The magnitude of wave-induced BSS is defined as the following (Soulsby, 1995):

$$\tau_{wave} = 0.5\rho f_w u_{wave}^{\ 2} \qquad \text{(A.8)}$$

where u_{wave} is the root-mean-square value of the maximum orbital motion near the bottom. This was part of the output from the SWAN models applied to both sites. The parameter f_w is a friction factor for waves:

$$f_w = 1.39\left(\frac{\xi}{k_s/30}\right)^{-0.52} \qquad \text{(A.9)}$$

in which ξ is particle excursion amplitude near the bed, which was also part of the output from the SWAN models.

An example of modelled tidal current, wave height as well as τ_c and τ_w is shown in Fig. A.3. Stations Z7 and B2 were chosen for demonstration and comparison purposes since these two stations have similar elevations (i.e. 0.3–0.45 m NAP for Z7 and 0.2–0.3 m NAP for B2). It is clear that the water level fluctuation is similar at both stations. The tidal current velocity and associated τ_c are slightly stronger at station Z7 compared with station B2, whereas the wave height and τ_c are much larger at station Z7 compared with station B2.

The mean BSS in a wave cycle under combined waves and currents is calculated as the following (Soulsby, 1995):

$$\tau_m = \tau_{cur}\left[1+1.2\left(\frac{\tau_{wave}}{\tau_{cur}+\tau_{wave}}\right)^{3.2}\right] \quad \text{(A.10)}$$

The maximum BSS in a wave cycle is calculated as the following (Soulsby, 1995):

$$\tau_{\max} = \left[(\tau_m + \tau_{wave}|\cos\theta|)^2 + (\tau_{wave}|\sin\theta|)^2\right]^{0.5} \quad \text{(A.11)}$$

Appendix B. Spatial autocorrelation check

In the current study, correlation analysis between the spatial eigenfunctions of $\tau_{\max}$ and bed level dynamics was conducted to reveal the relation between BSS and intertidal morphodynamics. As any statistical analysis requires independent data sets, we performed spatial autocorrelation analysis of the obtained spatial eigenfunctions prior to correlation analysis. The spatial

autocorrelation level was measured by Moran's I (i.e. $I(d)$), which is a function of distance (d) between the monitoring station sequence (Fortin and Dale, 2005).

$$I(d) = \frac{\frac{1}{W}\sum_{i=1}^{n}\sum_{j=1}^{n} W_{ij}(x_i - \bar{x})(x_j - \bar{x})}{\frac{1}{n}\sum_{i=1}^{n}(x_i - \bar{x})^2} \quad \text{(B.1)}$$

where x_i and x_j are the spatial eigenfunction values at station i and j, respectively; $\bar{x}$ is the spatial mean value of all the n stations; $W_{ij} = 1$, when the distance between x_i and x_j is d; $W_{ij} = 0$, for all other cases; W is the sum of the W_{ij} matrix. If d=1, the examined data set is the original data set. If d=2, the examined data set is the data from every other station in the original data set. Based on Equation (B.1), the spatial autocorrelation level of the spatial eigenfunctions of τ_{max} and bed level dynamics was obtained (Table B.1).

If an original dataset has a Moran's I higher than 1/e or lower than -1/e, it needs to be subsampled to obtain an independent data set with a lower spatial autocorrelation level. At the Baarland site, the absolute values of Moran's I in both spatial eigenfunctions of τ_{max} and bed level dynamics were smaller than the 1/e threshold. This indicates the original datasets (with distance equal to 1) have a low level of autocorrelation(Fortin and Dale, 2005). Thus, these spatial eigenfunctions can be regarded as independent datasets ready for correlation analysis. For the Zuidgors site, however, the absolute values of Moran's I of the original spatial eigenfunctions were higher than the 1/e threshold. Therefore, these datasets were autocorrelated, and needed subsampling to generate independent data. Table B1 further shows that when the sampling distance increased to 2, the absolute values of Moran's I dropped below the 1/e threshold. Therefore, we used a subsampling distance of 2 to obtain independent datasets for the spatial eigenfunctions for correlation analysis at this site.

Figure and table Captions

Fig. 1. Conceptual diagram of the Dynamic Equilibrium Theory (DET) of tidal flats, as proposed by Friedrichs (2011). The patterns in bed shear stress (BSS) induced by tidal currents (τ_c) and waves (τ_w) result in contrasting spatial distributions of sediment across flats. Where bed shear stress is higher than the uniform BSS associated with tidal flat equilibrium (τ_E), erosion tends to occur. Where BSS is lower than τ_E, deposition tends to occur. The sediment distributions resulting from tidal and wave forcing lead to corresponding tide-dominated (convex) and wave-dominated (concave) profile shapes. With constantly changing BSS, an actual tidal flat typically lies somewhere between tide-dominated and wave-dominated profiles, and is driven towards one or the other extreme depending on the prevailing mode of hydrodynamic forcing.

Fig. 2. (a) Study sites in the Westerschelde estuary, southwestern Netherlands. (b) Suspended sediment concentration data in the estuary were collected at the Terneuzen SPM (Suspended Particulate Matter) station. (c) The Zuidgors site is exposed to waves, whereas the Baarland site is sheltered from waves because of the blockage of a seaward shoal. (d & e) Monitoring profiles at Zuidgors and Baarland are shown. The shown elevation was adjusted to the NAP (Normal Amsterdam Peil) reference. Note the 10-fold difference in the x-axis scale between panels d and e. The sticks inserted in the bed represent SED-sensors. Filled squares and open stars represent pressure sensors for wave measurement and ADCP for velocity measurement, respectively. Stations with open squares did not have pressure sensors installed.

Fig. 3. Bed-level position (blue dots and open circles) and combined maximum BSS due to tidal current and waves (τ_{max}, red lines) at the Zuidgors (exposed) and Baarland (sheltered) stations. The bed-level position of each station was set as zero at the beginning of the measurements. Blue dots represent the data measured by SED-sensors. When there were data gaps due to SED-sensor failure, monthly DGPS surveys (blue circles) were used as complementary data.

Fig. 4. (a & b) The 1st spatial eigenfunctions (e_1) of τ_c, τ_w and τ_{max} at the exposed Zuidgors and sheltered Baarland sites, respectively. The variable e_1 represents the primary component of the spatial variation in these forces. (c & d) The 1st temporal eigenfunctions (c_1) of τ_c, τ_w and τ_{max} at the two sites, respectively; c_1 represents the corresponding temporal components of e_1 in these forces.

Fig. 5. (a & b) Comparisons between the 1st spatial eigenfunctions (e_1) of τ_{max} and bed-level dynamics at the Zuidgors and the Baarland sites, respectively. (c & d) Comparisons between the 2nd spatial eigenfunctions (e_2) of τ_{max} and bed-level dynamics at the Zuidgors and the Baarland sites, respectively. The parameters e_1 and e_2 represent the two most important eigenfunctions describing spatial variation.

Fig. 6. Spectrum distribution of the temporal eigenfunctions of τ_{max} (a & b) and bed-level dynamics (c & d). Both the 1st and 2nd temporal eigenfunctions ($c_1(t)$ and $c_2(t)$) are shown. SP1-SP3 in (a) and (b) represent subordinate peaks in the spectrums.

Fig. 7. Reconstructed 1st modes (i.e. 1st combined eigenfunctions) of bed-level changes and τ_{max} at both sites (a-d), and reconstructed 2nd modes (i.e. 2nd combined eigenfunctions) of the bed-level changes and τ_{max} at both sites (e-h). The reconstructed 1st and 2nd modes represent the dominant meaningful signals of a data set. The percentage of variance explained by each mode is indicated in each panel. Please note the differing colour scales in each panel, and that for demonstration purposes, data points were interpolated between two stations.

Fig. A1. Comparison between the modelled and measured significant wave height (Hs). The shown data were obtained from all 9 wave stations at both sites (see Fig. 2 for station locations).

Fig. A2. Comparison between the modelled and measured velocity. The velocity data were obtained at 6 ADCP stations shown in Fig.2.

Fig. A3. Water level, tidal current velocity, significant wave height (H_s) as well as BSS induced by currents and waves at station Z7 of the Zuidgors site and station B2 of the Baarland site, in which tidal current velocity, H_s and BSS were derived by modelling. The locations of Z7 and B2 station are shown in Fig.2.

Table 1. Relative contribution of mode *k* to the total variability (p_k)

Table B1. Moran's I values of the spatial eigenfunctions of $\tau_{\max}$ and bed level dynamics at both sites.

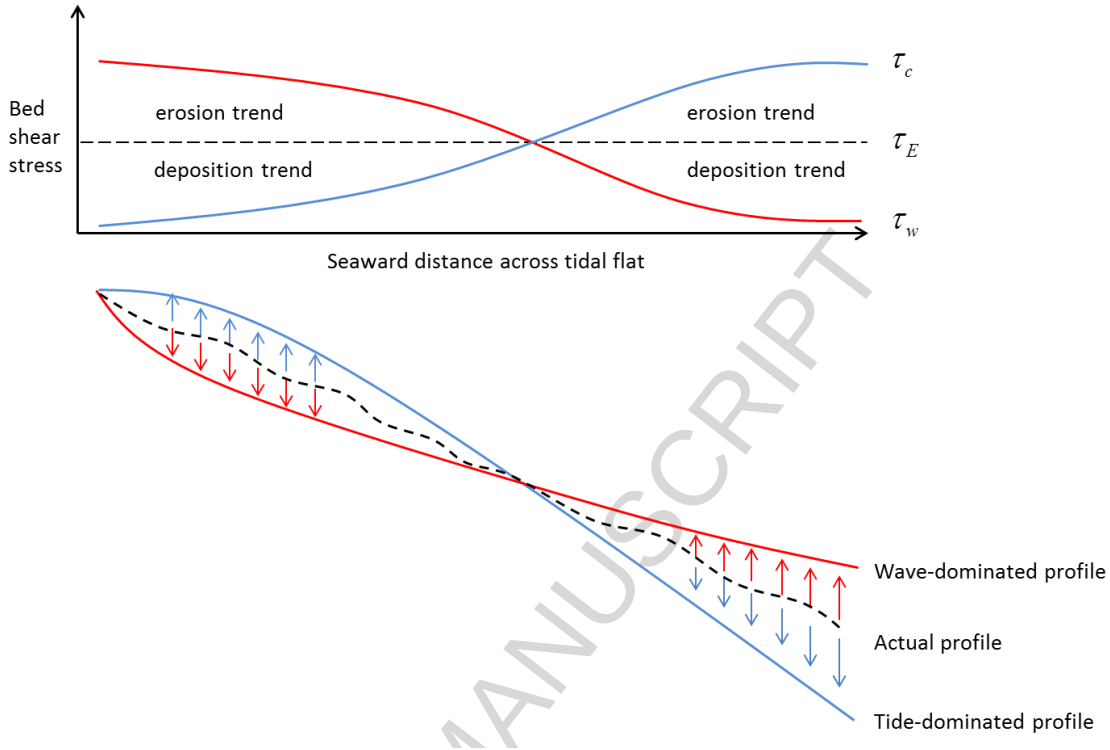

Fig. 1. Conceptual diagram of the Dynamic Equilibrium Theory (DET) of tidal flats, as proposed by Friedrichs (2011). The patterns in bed shear stress (BSS) induced by tidal currents (τ_c) and waves (τ_w) result in contrasting spatial distributions of sediment across flats. Where bed shear stress is higher than the uniform BSS associated with tidal flat equilibrium (τ_E), erosion tends to occur. Where BSS is lower than τ_E , deposition tends to occur. The sediment distributions resulting from tidal and wave forcing lead to corresponding tide-dominated (convex) and wave-dominated (concave) profile shapes. With constantly changing BSS, an actual tidal flat typically lies somewhere between tide-dominated and wave-dominated profiles, and is driven towards one or the other extreme depending on the prevailing mode of hydrodynamic forcing.

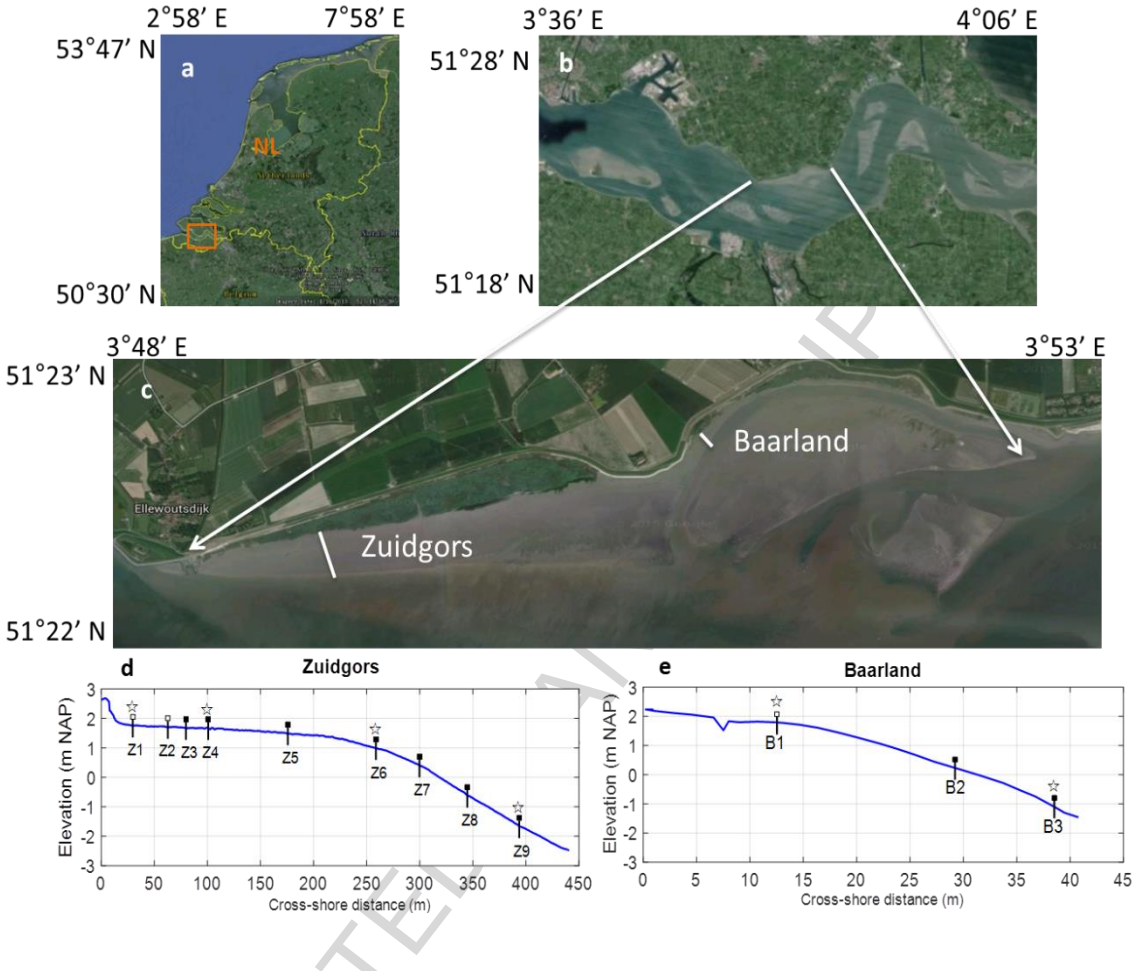

Fig. 2. (a) Study sites in the Westerschelde estuary, southwestern Netherlands. (b) Suspended sediment concentration data in the estuary were collected at the Terneuzen SPM (Suspended Particulate Matter) station. (c) The Zuidgors site is exposed to waves, whereas the Baarland site is sheltered from waves because of the blockage of a seaward shoal. (d & e) Monitoring profiles at Zuidgors and Baarland are shown. The shown elevation was adjusted to the NAP (Normal Amsterdam Peil) reference. Note the 10-fold difference in the x-axis scale between panels d and e. The sticks inserted in the bed represent SED-sensors. Filled squares and open stars represent pressure sensors for wave measurement and ADCP for velocity measurement, respectively. Stations with open squares did not have pressure sensors installed.

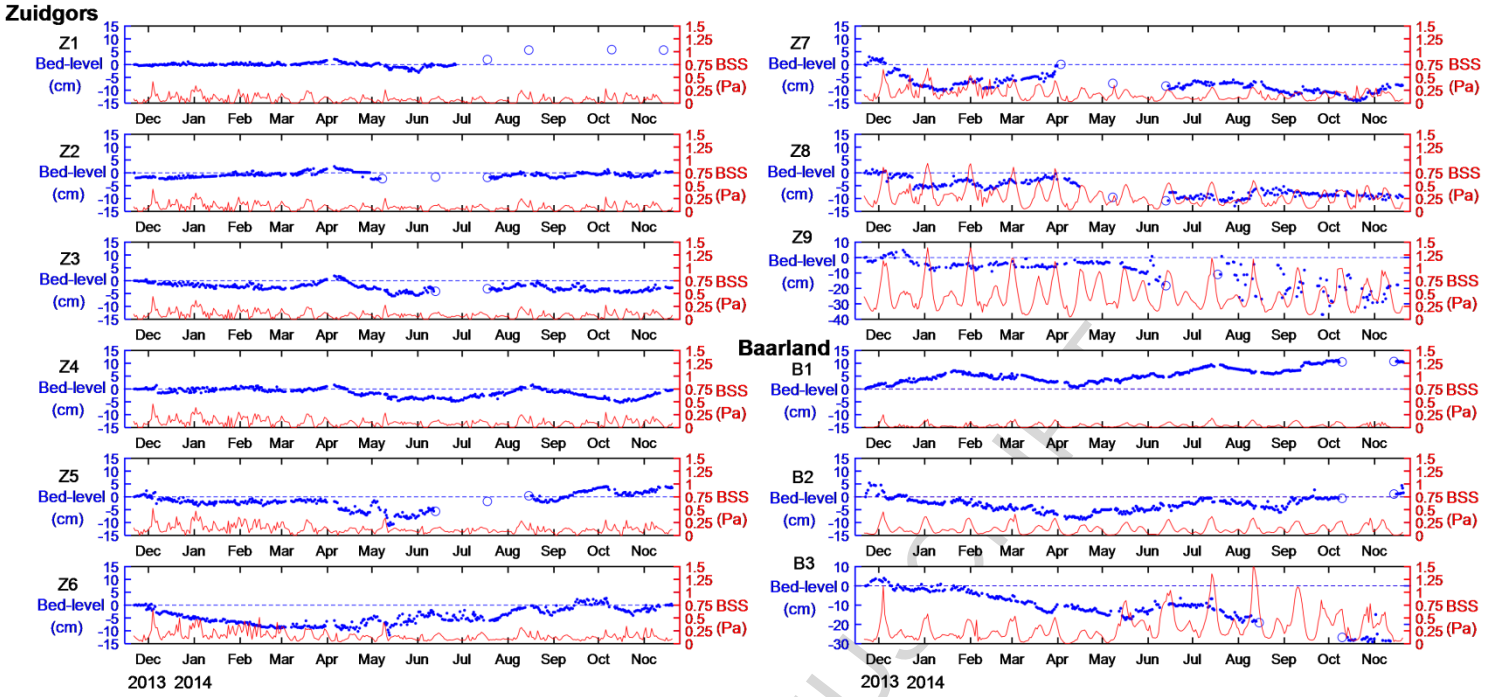

Fig. 3. Bed-level position (blue dots and open circles) and combined maximum BSS due to tidal current and waves (τ_{max}, red lines) at the Zuidgors (exposed) and Baarland (sheltered) stations. The bed-level position of each station was set as zero at the beginning of the measurements. Blue dots represent the data measured by SED-sensors. When there were data gaps due to SED-sensor failure, monthly DGPS surveys (blue circles) were used as complementary data.

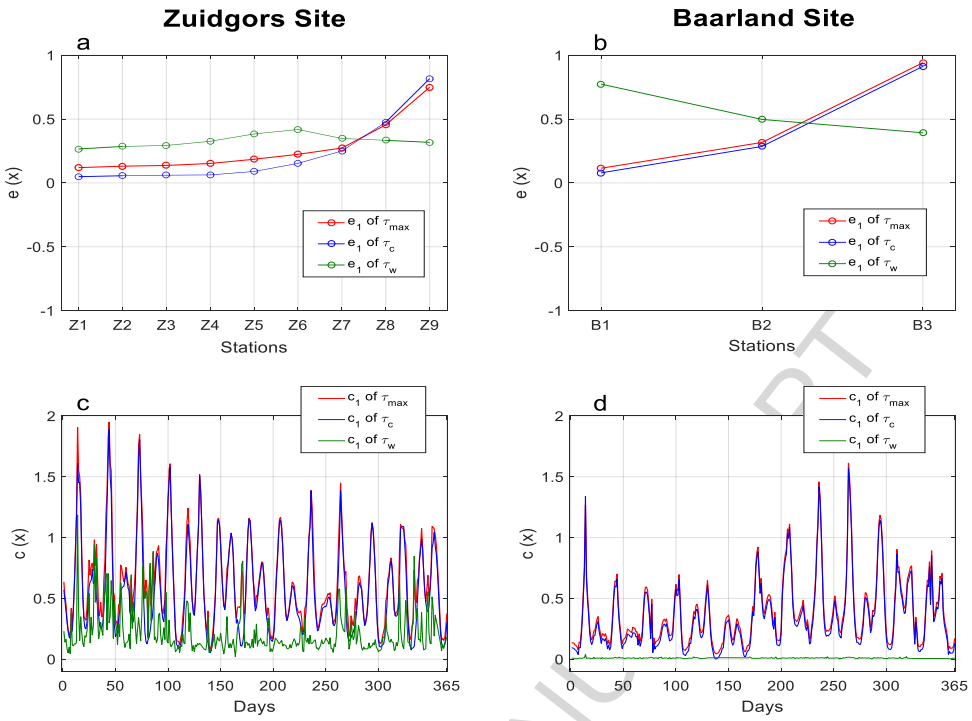

Fig. 4. (a & b) The 1st spatial eigenfunctions (e_1) of τ_c, τ_w and τ_{max} at the exposed Zuidgors and sheltered Baarland sites, respectively. The variable e_1 represents the primary component of the spatial variation in these forces. (c & d) The 1st temporal eigenfunctions (c_1) of τ_c, τ_w and τ_{max} at the two sites, respectively; c_1 represents the corresponding temporal components of e_1 in these forces.

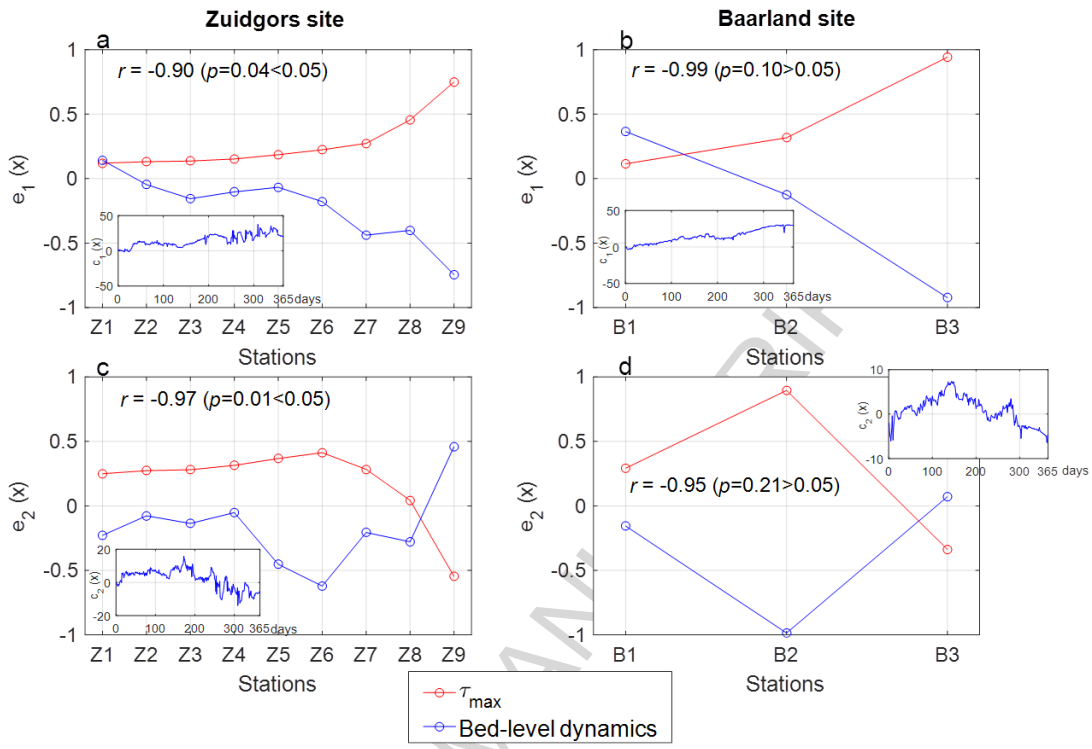

Fig. 5. (a & b) Comparisons between the 1st spatial eigenfunctions (e_1) of τ_{max} and bed-level dynamics at the Zuidgors and the Baarland sites, respectively. (c & d) Comparisons between the 2nd spatial eigenfunctions (e_2) of τ_{max} and bed-level dynamics at the Zuidgors and the Baarland sites, respectively. The parameters e_1 and e_2 represent the two most important eigenfunctions describing spatial variation.

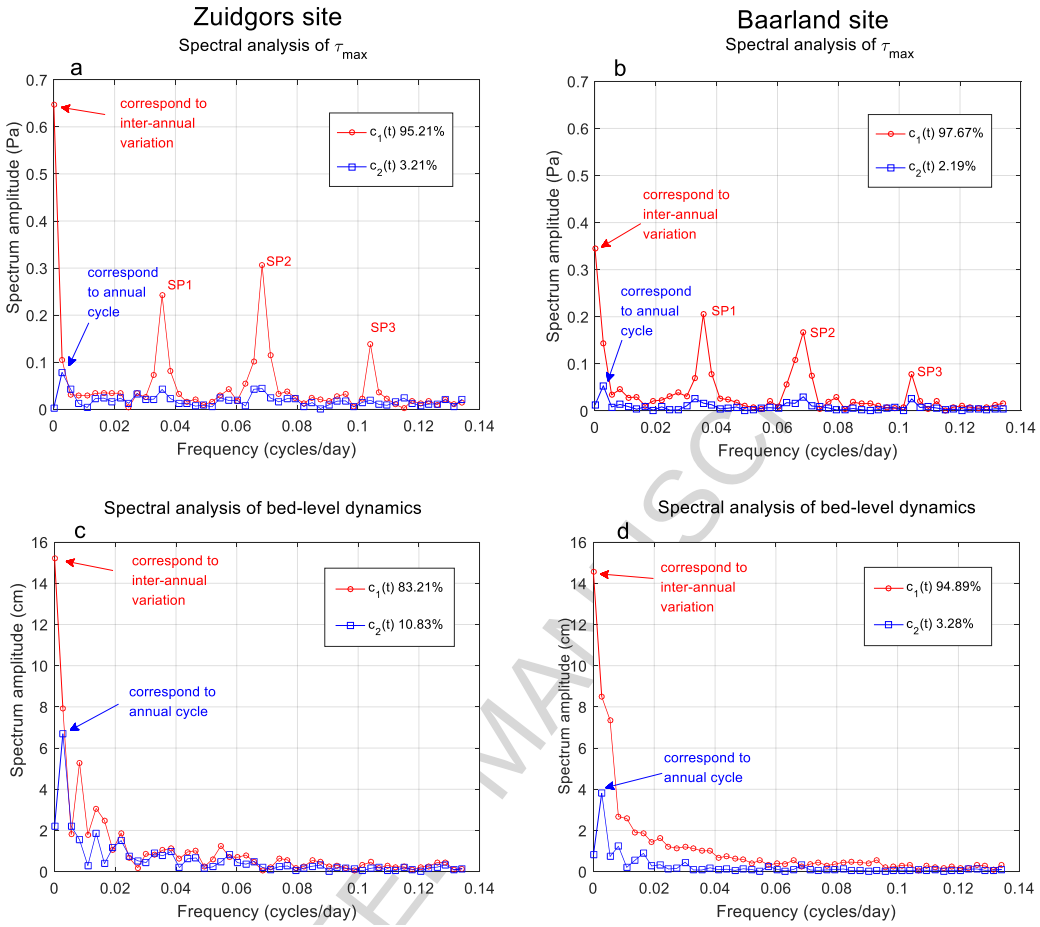

Fig. 6. Spectrum distribution of the τ_{max} temporal eigenfunctions (a & b) and bed-level dynamics temporal eigenfunctions (c & d). Both the 1st and 2nd temporal eigenfunctions (c_1(t) and c_2(t)) are shown. SP1-SP3 in (a) and (b) represent subordinate peaks in the τ_{max} spectrum.

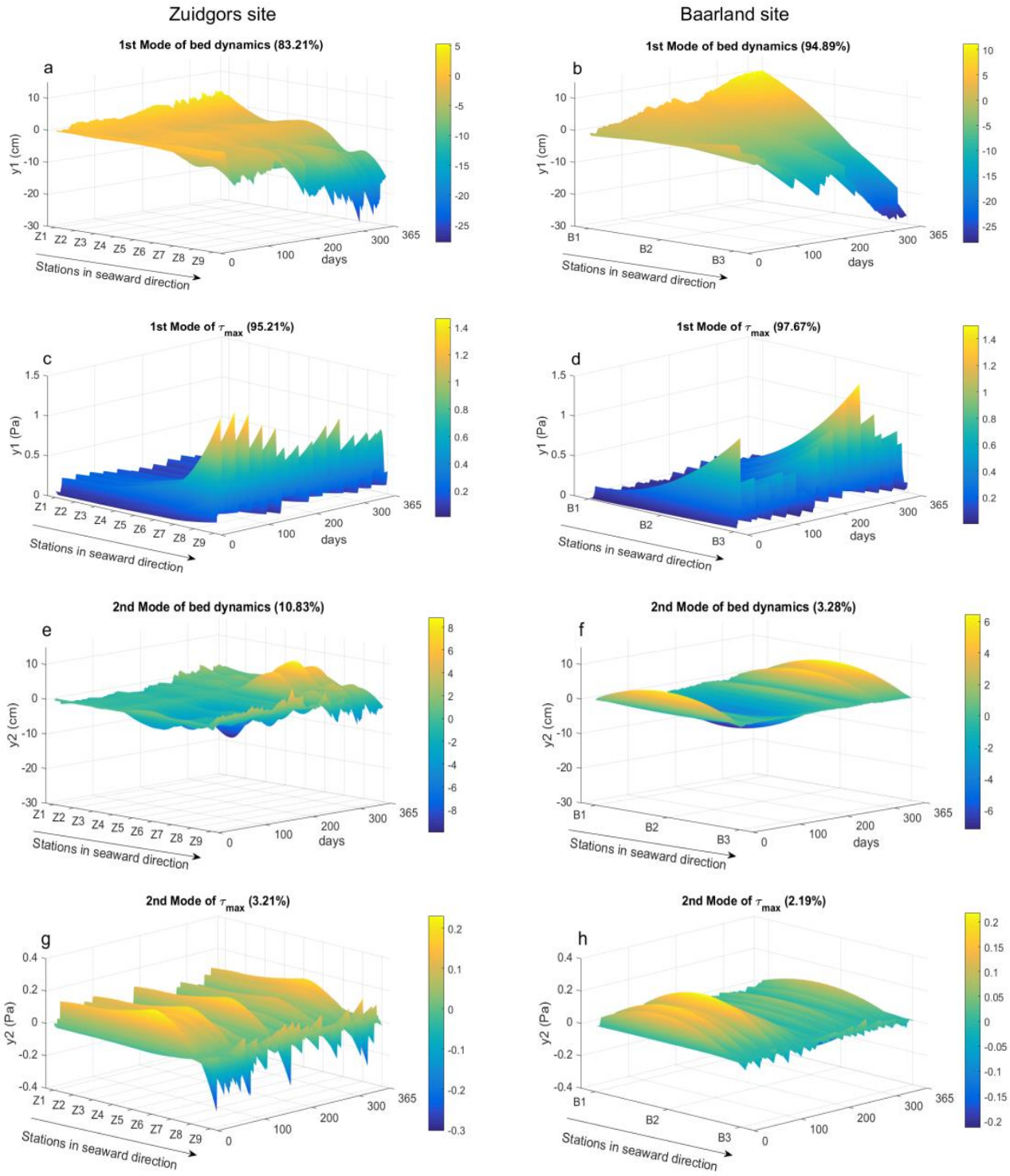

Fig. 7. Reconstructed 1st modes (i.e. 1st combined eigenfunctions) of bed-level changes and τ_{max} at both sites (a-d), and reconstructed 2nd modes (i.e. 2nd combined eigenfunctions) of the bed-level changes and τ_{max} at both sites (e-h). The reconstructed 1st and 2nd modes represent the dominant meaningful signals of a data set. The percentage of variance explained by each mode is indicated in each panel. Please note the differing colour scales in each panel, and that for demonstration purposes, data points were interpolated between two stations.

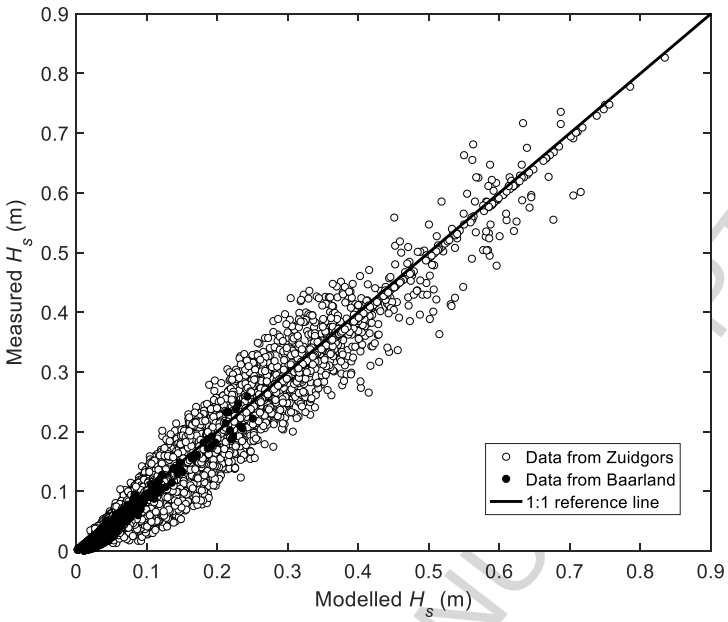

Fig. A1. Comparison between the modelled and measured significant wave height (Hs). The shown data were obtained from all 9 wave stations at both sites (see Fig. 2 for station locations).

Fig. A2. Comparison between the modelled and measured velocity. The velocity data were obtained at 6 ADCP stations shown in Fig.2.

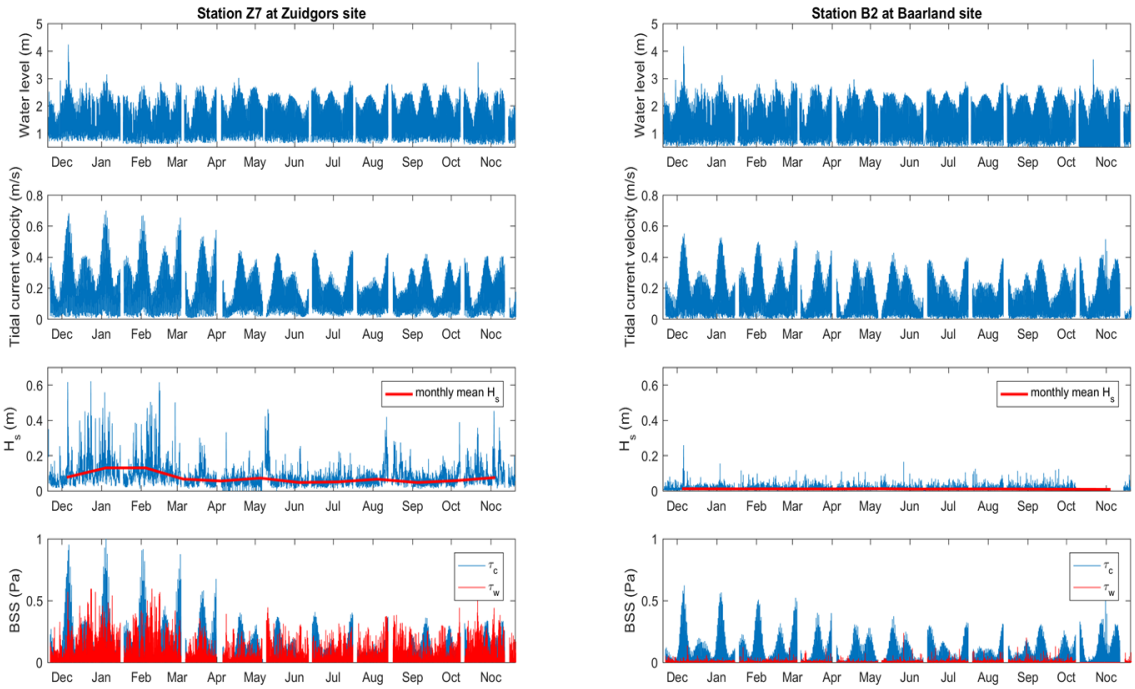

Fig. A3. Water level, tidal current velocity, significant wave height (H_s) as well as BSS induced by currents and waves at station Z7 of the Zuidgors site and station B2 of the Baarland site, in which tidal current velocity, H_s and BSS were derived by modelling. The locations of Z7 and B2 station are shown in Fig.2.

Table 1. Relative contribution of mode k to the total variability (p_k)

Data set	Percent variance explained (p_k)			
	e1(x)	e2(x)	e3(x)	Remaining
Zuidgors, bed dynamics	83.21%	10.83%	2.35%	3.61%
Zuidgors, $\tau_{\max}$	95.21%	3.21%	1.01%	0.57%
Zuidgors, τ_c	98.12%	1.46%	0.33%	0.09%
Zuidgors, τ_w	88.37%	8.56%	1.41%	1.66%
Baarland, bed dynamics	94.89%	3.28%	1.83%	-
Baarland, $\tau_{\max}$	97.67%	2.19%	0.14%	-
Baarland , τ_c	97.66%	2.18%	0.16%	-
Baarland, τ_w	89.76%	9.34%	0.90%	-

Table B1. Moran's I values of the spatial eigenfunctions of τ_{max} and bed level dynamics at both sites.

Item	Zuidgors		Baarland
Distance (d)	1	2	1
τ_{max}	0.4791	0.1391	-0.0756
Bed-level dynamics	0.3911	0.1315	-0.1044